HHS Public Access

Author manuscript

Magn Reson Med. Author manuscript; available in PMC 2016 October 01.

Published in final edited form as:

Magn Reson Med. 2015 October ; 74(4): 1019–1031. doi:10.1002/mrm.25487.

Integrated Image Reconstruction and Gradient Nonlinearity Correction

Shengzhen Tao[1], **Joshua D. Trzasko**[2], **Yunhong Shu**[2], **John Huston III**[2], and **Matt A. Bernstein**[2]

[1]Mayo Graduate School, Mayo Clinic, Rochester, MN, USA

[2]Department of Radiology, Mayo Clinic, Rochester, MN, USA

Abstract

Purpose—To describe a model-based reconstruction strategy for routine magnetic resonance imaging (MRI) that accounts for gradient nonlinearity (GNL) during rather than after transformation to the image domain, and demonstrate that this approach reduces the spatial resolution loss that occurs during strictly image-domain GNL-correction.

Methods—After reviewing conventional GNL-correction methods, we propose a generic signal model for GNL-affected MRI acquisitions, discuss how it incorporates into contemporary image reconstruction platforms, and describe efficient non-uniform fast Fourier transform (NUFFT)-based computational routines for these. The impact of GNL-correction on spatial resolution by the conventional and proposed approaches is investigated on phantom data acquired at varying offsets from gradient isocenter, as well as on fully-sampled and (retrospectively) undersampled *in vivo* acquisitions.

Results—Phantom results demonstrate that resolution loss that occurs during GNL-correction is significantly less for the proposed strategy than for the standard approach at distances >10 cm from isocenter with a 35 cm FOV gradient coil. The *in vivo* results suggest that the proposed strategy better preserves fine anatomical detail than retrospective GNL-correction while offering comparable geometric correction.

Conclusion—Accounting for GNL during image reconstruction allows geometric distortion to be corrected with less spatial resolution loss than is typically observed with the conventional image domain correction strategy.

Keywords

Model-based Reconstruction; Gradient Nonlinearity; Nonuniform Fast Fourier Transform

Introduction

Conventional clinical magnetic resonance imaging (MRI) operates under the assumption that spatial encoding gradients vary linearly across the imaging field-of-view (FOV). Due to

Please direct all correspondences to: Matt A. Bernstein, Ph.D., Mayo Clinic, 200 First Street SW, Rochester, MN 55905, USA, Phone: +1 507 266 1207, Fax: +1 507 266 1657, mbernstein@mayo.edu.

engineering constraints on system efficiency and coil performance, realizing linear gradient across the entire FOV is not always feasible. Moreover, sacrificing some gradient linearity for increased gradient amplitude and slew rate capabilities may help relax amplifier requirements or reduce peripheral nerve stimulation (1). MR image reconstruction methods (e.g., inverse Fourier transform) typically assume that the acquired data set was spatially encoded using linear gradients, so the presence of gradient nonlinearity (GNL) causes geometric distortion in the generated MR images due to mismapping between the nominal and actual data acquisition models (2). In applications that require high geometric accuracy, such as pre-surgical or radiation treatment planning and longitudinal, multicenter studies, such geometric infidelity can be particularly problematic (3–7).

Standard GNL-correction techniques, such as those widely available on commercial MR systems (e.g., "gradwarp" on General Electric systems), are implicitly based on the assumption that an infinite set of continuous, noise-free *k*-space samples was acquired (8). In this case, following inverse (continuous) Fourier transformation of the data set, the nominal and actual images of the continuous physical object are related by a (continuous, conformal) coordinate mapping and intensity scaling based on the mapping's Jacobian determinant (4). Presuming that this mapping is both *a priori* known and bijective (i.e., invertible), the actual object image can be recovered from the distorted one simply by inverting these operations. In practice, however, only a finite set of discrete samples is acquired, and image-domain interpolation is used to approximate the coordinate mapping operation (2, 4, 8, 9).

In practice, there are several challenges associated with the image-based interpolation GNL-correction. Due to the intrinsic smoothing effect of interpolation, blurring or resolution loss is expected to occur (10). This effect can be somewhat reduced by employing more advanced interpolation models, but not wholly eliminated (10, 11). Furthermore, image discretization can also be problematic, particularly when GNL causes the target object to shrink substantially and force a large amount of information into only a few pixels or even a single pixel. Additionally, standard GNL-correction methods do not explicitly account for the presence of noise, undersampling, or other reconstruction artifacts (e.g., from parallel imaging) in the initial image data, and are thus subject to error propagation and amplification.

Artifacts manifest whenever an image reconstruction model is used that does not accurately describe the data to which it is being applied. Prospectively accounting for MRI system non-idealities during image reconstruction – rather than attempting to retrospectively correct them after transformation into the image domain – is a paradigm that may be logically appealing and has already shown some success in other areas of MRI, such as off-resonance correction (12) and chemical shift-encoded imaging (13). In the context of GNL-correction, prospective correction strategies have previously been considered for acquisitions scenarios where spatial encoding gradients are intentionally distorted (e.g., PATLOC), but this approach has not yet been considered for the more common scenario where ideally linear gradients are not performing as desired due to engineering limitations (14, 15).

In this work, we investigate how prospectively accounting for gradient linearity during image reconstruction can be beneficial even in routine imaging cases where gradients

unintentionally deviate from linearity. Although we focus on 2D Cartesian imaging, the same methodology can be applied to 3D or non-Cartesian cases. After defining a generic signal model for MRI data acquisition, we describe a model-based inverse problem framework for performing GNL-aware MR image reconstruction for both non-accelerated and accelerated scans. Both non-iterative and iterative computational methods will be discussed. Several phantom and *in vivo* scan examples, with varying degrees of GNL-distortion, are analyzed. Finally, several extensions and generalizations of the proposed framework are discussed.

Theory

Standard GNL-Correction

Standard GNL-correction operates under the assumption that continuous, infinite, noise-free MRI data are available. Let $\Delta(\mathbf{x})$ denote the presumed *a priori* known mapping from nominal to actual spatial encoding position that results from GNL. Then, the observed MRI signal at any *k*-space position, $\mathbf{k}$, can be modeled as:

$$g(\mathbf{k}) = \int_{\Omega} f(\mathbf{x}) e^{-j2\pi \cdot \mathbf{k} \cdot \Delta(\mathbf{x})} d\mathbf{x}, \quad [1]$$

where f is a continuous function representing the imaged object, $\mathbf{x}$ denotes (true) spatial position, and Ω is the field of excitation (FOX). Note that Eq. 1 is simply the continuous Fourier transform of f when $\Delta(\mathbf{x}) = \mathbf{x}$. It is then presumed that image reconstruction is performed via inverse Fourier Transform (iFT):

$$\tilde{f}(\mathbf{x}') = \int_{W} g(\mathbf{k}) e^{j2\pi \cdot \mathbf{k} \cdot \mathbf{x}'} d\mathbf{k} = \int_{W} \int_{\Omega} f(\mathbf{x}) e^{j2\pi \cdot \mathbf{k} \cdot [-\Delta(\mathbf{x}) + \mathbf{x}']} d\mathbf{x} d\mathbf{k}, \quad [2]$$

where W denotes the *k*-space support of signal g. If the distortion field, $\Delta(\mathbf{x})$, is bijective and thus invertible, applying a change of variables to the above yields the following:

$$\tilde{f}(\mathbf{x}') = \int_{W} \int_{\Omega} f\left(\overrightarrow{\Delta}^{-1}(\mathbf{x}'')\right) e^{j2\pi \cdot \mathbf{k} \cdot [-\mathbf{x}'' + \mathbf{x}']} \left| \frac{\partial \overrightarrow{\Delta}^{-1}(\mathbf{x}'')}{\partial \mathbf{x}''} \right| d\mathbf{x}'' d\mathbf{k} = f\left(\overrightarrow{\Delta}^{-1}(\mathbf{x}')\right) \left| \frac{\partial \overrightarrow{\Delta}^{-1}(\mathbf{x}')}{\partial \mathbf{x}'} \right|, \quad [3]$$

where, $\tilde{f}$ is the distorted (continuous) image, Δ^{-1} denotes the inverse function of distortion field, and $\left| \frac{\partial \Delta^{-1}(\mathbf{x}')}{\partial \mathbf{x}'} \right|$ is the Jacobian determinant of $\Delta^{-1}(\cdot)$.

From Eq. 3, an image acquired under GNL and reconstructed via conventional Fourier transform methods will exhibit both geometric spatial distortion and intensity modulation. It similarly follows that the distortion-free actual image can, in theory, be recovered from the reconstructed one by applying a point-wise intensity correction along with a continuous-to-continuous bijective coordinate mapping, i.e.,

$$f(\mathbf{x}) = \tilde{f}(\vec{\Delta}(\mathbf{x})) \cdot \left| \frac{\partial \vec{\Delta}(\mathbf{x})}{\partial \mathbf{x}} \right|. \quad [4]$$

In reality, only a finite set of *k*-space samples is available, and the reconstructed image is also of limited size. Practically, the bijective mapping is approximated using a discrete interpolation operation. The standard discrete analog of Eq. 4 is thus:

$$\mathbf{f}[\mathbf{i}] = \mathbf{J} \cdot \mathbf{Q}_{\Delta} \cdot \tilde{\mathbf{f}}[\mathbf{i}] \quad [5]$$

where **i** is the pixel index, $\tilde{\mathbf{f}}$ [**i**] and **f** [**i**] represent the distorted and corrected image matrices, respectively, $\mathbf{Q}_{\Delta}$ represents the interpolation kernel (e.g., cubic spline), and **J** denotes pixel-wise scaling by Jacobian determinant of distortion field. Note that $\mathbf{Q}_{\Delta}$ is not necessarily invertible even if Δ(**x**) is bijective due to the implicit discretization of this field inside the linear operator. The accuracy of data interpolation is determined by the type of interpolation kernel and the sampling grid density. Commonly used spatial interpolation kernels usually satisfy certain spatial smoothness conditions and therefore impart blurring in the corrected images. In addition, due to practical limits on imaging resolution and pixel size, the accuracy of interpolation is further degraded. Thus, Eq. 5 deviates from the theoretical prediction in Eq. 4 and resolution loss can be expected.

Proposed Signal Model

In practice only a finite number of *k*-space samples can be collected and will contain noise. Accounting for these realities, the MRI data acquisition model in Eq. 1 can be modified as:

$$\mathbf{g}[\kappa] = \int_{\Omega} f(\mathbf{x}) e^{-j w[\kappa] \cdot \Delta(\mathbf{x})} d\mathbf{x} + \mathbf{n}[\kappa], \quad [6]$$

where **g** represents the discrete measurement vector, κ is the *k*-space sample index, and **n**[κ] is an instance of proper complex gaussian noise in the κ-th sample point (16). Note the presence of noise in the proposed signal model as opposed to the signal model of the standard GNL-correction in Eq. 1.

Like before, GNL-correction corresponds to the inverse problem of reconstructing image *f*(**x**) given a set of *k*-space samples, **g**. In the absence of auxiliary assumptions, this problem is intrinsically ill-posed since a continuous function is to be estimated from discrete measurements. A standard solution is to approximate the function *f*(**x**) via finite series representation, i.e., $f(\mathbf{x}) \approx \Sigma_{i \in \Theta} \mathbf{u}[i] b(\mathbf{x} - \mathbf{r}[i])$, where *i* is the pixel index, **u**[*i*] is the display coefficient of the *i*-th pixel, *b* is the pixel basis model, and **r**[*i*] denotes the actual spatial position of the *i*-th pixel (17). Assuming a Dirac delta pixel model, the forward signal model in Eq. 6 becomes

$$\mathbf{g}[\kappa] = \sum_{i \in \Theta} \int_{\Omega} \mathbf{u}[i] \delta(\mathbf{x} - \mathbf{r}[i]) e^{-j w[\kappa] \cdot \Delta(\mathbf{x})} d\mathbf{x} + \mathbf{n}[\kappa] = \sum_{i \in \Theta} \mathbf{u}[i] e^{-j w[\kappa] \cdot \Delta(\mathbf{r}[i])} + \mathbf{n}[\kappa]; \quad [7]$$

Denoting the nominal spatial position $\mathbf{r}'[i] = \Delta(\mathbf{r}[i])$ and defining the forward matrix operator $\mathbf{A}[\kappa, i] = e^{-jw\longrightarrow[\kappa]\cdot\mathbf{r}'[i]}$, the ensemble of measured data can be modeled in affine algebraic form as:

$$\mathbf{g}=\mathbf{A}\mathbf{u}+\mathbf{n}. \quad [8]$$

For (non-accelerated) Cartesian imaging, the set of *k*-space samples lie on a discrete uniform grid. Although image pixels are also generally assumed to lie on a similar uniform grid ($\mathbf{r}[i]$), the presence of distortion field (i.e., when $\Delta(\mathbf{r}[i]) \neq \mathbf{r}[i]$ in Eq. 8) causes these to be displaced in the discrete forward model according to $\Delta(\mathbf{r}[i])$. Therefore, the nominal spatial grid of an image reconstructed under Eq. 8 may actually be non-uniform. Thus, **A** essentially represents a non-uniform-to-uniform linear mapping for the Cartesian case. Note that without gradient nonlinearity, i.e., $\Delta(\mathbf{r}[i]) = \mathbf{r}[i]$, the forward operator **A** reverts to the standard discrete Fourier transform (DFT) matrix.

The forward operator, **A** in Eq. 8 can be efficiently implemented via the type I nonuniform fast Fourier transform (NUFFT) (18). NUFFTs of various types have previously been used for image reconstruction in other MRI areas such as non-Cartesian (19, 20) imaging, as well as for PATLOC (14, 21) and O-space (15) imaging where nonlinear and non-bijective spatial encoding gradients are intentionally introduced to offer improved encoding efficiency. The type I NUFFT, **A**, is defined as follows:

$$\mathbf{A}=\mathbf{D}\mathbf{F}\mathbf{\Gamma} \quad [9]$$

where $\mathbf{\Gamma}$ is a matrix representing convolution interpolation operation that maps the irregular image grid onto an oversampled uniform image grid, **F** is an oversampled DFT (implemented via fast Fourier transform (FFT)), and **D** is pixel-wise deapodization function (i.e., diagonal matrix) that compensates for blurring induced by convolutional kernel, $\mathbf{\Gamma}$.

General Reconstruction Strategy for Cartesian MRI

MRI data are usually acquired with multiple coils and receiver channels. Additionally, undersampling (i.e., collected only a subset of the data normally obtained during a scan) is commonly performed to reduce overall scan time. Let *K, C* and *N* denote the total numbers of *k*-space samples, receiver coils, and pixels in the reconstructed image, respectively. For the general case, the signal model in Eq. 8 extends to:

$$\mathbf{G}=\mathbf{\Phi}\mathbf{A}\mathbf{U}+\mathbf{N}. \quad [10]$$

where **G** is $K \times C$ measurement matrix, $\mathbf{\Phi}$ is the $K \times N$ binary row selection matrix that indicates the subset of Fourier elements actually sampled during the exam, **U** is the targeted underlying multi-channel image set ($N \times C$), and **N** is again proper complex Gaussian noise matrix ($K \times C$) which is herein assumed uncorrelated for simplicity.

A common strategy for reconstructing both fully- and undersampled MRI data is penalized regression, which seeks to produce the image most likely to have produced the set of noisy

measurements while potentially also satisfying some other expected properties (e.g., sparsity) (17). Since noise in MRI is Gaussian distributed, penalized least squares regression of the following general form is often employed:

$$\{\hat{\mathbf{U}}\}=\arg\min_{\mathbf{U}\in\mathbb{C}^{N\times C}}\{\lambda P(\mathbf{U})+\|\,\Phi\mathbf{A}\mathbf{U}-\mathbf{G}\,\|_F^2\} \quad [11]$$

where $\|\cdot\|_F^2$ is the Frobenius norm of matrix, $P(\cdot)$ is a regularization or penalty functional that promotes some desired property in the reconstructed image, and $\lambda \geq 0$ is a mixing parameter that controls the relative preference placed onto the penalty functional and the data fidelity term, $\|\,\Phi\mathbf{A}\mathbf{U}-\mathbf{G}\,\|_F^2$. Note that Jacobian-based intensity correction is not an explicit part of this model, as its effect is implicitly accounted for in the forward signal model. Also, note that Eq. 11 prospectively accounts for the presence of data noise; and for the special case of $\lambda = 0$, it provides the maximum likelihood estimate of **U**. Moreover, Tiknonov and locally low rank (LLR) (22) penalties can be included (via specific definition of $P(\mathbf{U})$) to provide robustness and stability when reconstructing undersampled data sets collected during accelerated scans.

Incorporating GNL-Correction into Some Common Reconstruction Strategies

Several common MR image reconstruction strategies arise from special instances of Eq. 11. For example, when no undersampling ($\mathbf{\Phi} = \mathbf{I}$) or regularization ($\lambda = 0$) is used, Eq. 11 reduces to ordinary least squares regression and has a simple closed form solution given by

$$\{\hat{\mathbf{U}}\}=\arg\min_{\mathbf{U}\in\mathbb{C}^{N\times C}}\{\|\,\mathbf{A}\mathbf{U}-\mathbf{G}\,\|_F^2\}=(\mathbf{A}*\mathbf{A})^{-1}\mathbf{A}*\mathbf{G} \quad [12]$$

which can be iteratively solved via standard or conjugate gradient (CG) descent. As will demonstrated later, the inverse Gramian matrix, $(\mathbf{A}^*\mathbf{A})^{-1}$, can be well approximated by a diagonal matrix built from the Jacobian determinant of distortion field (**J**), which in turn provides a non-iterative pathway for performing coil-by-coil GNL-corrected reconstruction of fully-sampled Cartesian MRI data:

$$\{\hat{\mathbf{U}}\}\approx\{\hat{\mathbf{U}}_{approx}\}=\mathbf{J}\mathbf{A}*\mathbf{G}. \quad [13]$$

The approximate solver in Eq. 13 and the standard GNL-correction strategy in Eq. 5 are functionally similar. The key difference is that the non-iterative method based on the proposed signal model utilizes explicit oversampled interpolation and deapodization steps, which enables later performing coarse geometric distortion correction without introducing substantial image blurring.

Beyond simple direct Fourier reconstruction, the proposed strategy also readily incorporates into standard SENSE-type reconstructions for accelerated acquisitions. Assume that the sensitivity profiles for the C channels of the phased array receiver are *a priori* known and contained within the $N \times C$ matrix, **S**. Then, the target signal in Eq. 11 can be reduced to

$$\mathbf{U}=diag\{\mathbf{u}\}\,\mathbf{S} \quad [14]$$

where $diag\{\mathbf{u}\}$ constructs an $N \times N$ diagonal matrix from the $N \times 1$ vector $\mathbf{u}$, which represents the target non-modulated image (23). Tikhonov-regularized SENSE ($P(\cdot)=\|\cdot\|_2^2$), for example, then involves solving:

$$\{\hat{\mathbf{u}}\}=\arg\min_{\mathbf{u}}\lambda\|\mathbf{u}\|_2^2+\|\Phi\mathbf{A}\,diag\{\mathbf{u}\}\,\mathbf{S}-\mathbf{G}\|_F^2, \quad [15]$$

which can be efficiently performed via linear CG iteration regardless of where uniform or non-uniform (i.e., random) sampling was performed. Eq. 15 inherently requires sensitivity profiles that are free from GNL-distortion. A simple way to provide this information is to perform sensitivity calibration in the usual fashion and then GNL-correct the estimated profiles via either Eq. 12 or Eq. 13.

The proposed gradient nonlinearity model can also be used within nonlinear reconstruction paradigms like CLEAR (24), a calibrationless parallel imaging method that utilizes LLR penalty functionals in lieu of explicit sensitivity profiles. CLEAR reconstruction operates by solving

$$\{\hat{\mathbf{U}}\}=\arg\min_{\mathbf{U}}\{\lambda\sum_{b\in\eta}\|\mathbf{R}_b\mathbf{U}\|_*+\|\Phi\mathbf{A}\mathbf{U}-\mathbf{G}\|_F^2\} \quad [16]$$

where $\|\cdot\|_*$ denotes the matrix nuclear norm, η defines a set of (potentially overlapping) spatial blocks, b is a block index, and $\mathbf{R}_b$ extracts a block indexed at b from each of the coil images. Nonsmooth convex optimization problems of this form can be readily solved using first-order methods like projected gradient (PG) iteration (22). Methods based on sparsity or low-rankedness like the above CLEAR example are typically applied for randomly undersampled acquisitions, i.e., where $\mathbf{\Phi}$ operates by selecting a random subset of the rows of $\mathbf{A}$.

Methods

The distortion field induced by GNL can be obtained in a variety of ways. Standard strategies on commercial MR system (e.g., “gradwarp”) rely on a parameterization of gradient field that can be obtained by electromagnetic field simulation, onsite measurement of the magnetic field (25), or measured via data fitting method using specialized phantom designed to track spatial distortion (6, 26–28). Alternatively, strategies making use of geometric information acquired from other modalities like CT are also available (4, 29). In this work, the vendor-provided parameterization of the distortion field was used.

Phantom and *In Vivo* Experiments

All experiments were performed on a 3.0 T scanner (General Electric, Signa HDxt system, v16.0) using the zoom mode gradient with maximum gradient amplitude and slew rates of 40 mT/m and 200 T/m/sec, and a 350 mm FOV, if not otherwise specified. The use of the

zoom mode, as opposed to the 480 mm FOV whole body mode allowed us to observe GNL-effects while minimizing the confounding effects of B_0 inhomogeneity. Fully-sampled *k*-space data were retained. The American College of Radiology (ACR) quality assurance (QA) phantom (30) was scanned using a single-channel head coil with a spin echo (SE) sequence. Pulse sequence acquisition parameters are summarized in Table 1. To compare the performance of the standard and proposed GNL-correction strategies at varying degree of gradient nonlinearity, image sets were acquired at each location as the phantom was translated in the Superior/Inferior (S/I) direction from -62 mm to -122 mm in increments of 5 mm (magnet coordinates; negative sign indicates the inferior direction). To demonstrate an example of large GNL distortion, a separate ACR phantom scan was performed at -235 mm in the S/I direction with the whole body coil and the 480 mm FOV whole body mode gradient with maximum gradient amplitude and slew rates of 23 mT/m and 80 T/m/sec. The whole body coil was used instead of the head coil because the slice location was far out of the coverage of the latter. Additionally, two healthy volunteers were scanned under an IRB-approved protocol using an 8-channel brain coil and the parameters listed in Table 1. The brain of one volunteer was scanned with a 3D MP-RAGE sequence, and a second with a 2D T_2-weighted Fast Spin Echo (FSE) sequence (echo train length = 12). A copy of the human *k*-space data was retrospectively undersampled for the different reconstruction experiments to further investigate the proposed method.

Data Processing

All data processing was performed on a dual 8-core 2.6 GHz machine with 128 GB memory. The reconstruction algorithms were implemented in C/C++ environment with FFTW and OpenMP parallelization. In this work, GNL-correction (all approaches) was performed only within 2D imaging plane. All standard image-domain GNL-corrections were executed using cubic spline interpolation. Unless noted otherwise, all NUFFT operations were implemented using 1.25 × oversampled FFT's and width 5 Kaiser-Bessel kernel interpolators (19, 20), and parallelized using thread privatization.

Reconstruction Experiments and Analysis

Initial analysis was performed to verify that the non-iterative method in Eq. 13 for fully-sampled Cartesian acquisitions provides an accurate approximation to the full iterative correction reconstruction in Eq. 12. GNL-correction of the high resolution (HR) insert plane (axial) of the ACR phantom was performed for two data sets corresponding to two different off-isocenter positionings of the phantom. Specifically, the physical location of the imaged section of the phantom was translated to -82 or -122 mm from gradient isocenter, in the S/I direction, and selected to exhibit mild and strong geometric distortion, respectively. Using the same acquisitions settings, another scan at -47 mm was performed twice, to enable imaging differencing and analysis of the effects of the different GNLC methods on noise power spectra. To demonstrate an example of extreme distortion, the phantom was further translated to -235 mm from gradient isocenter and scanned with whole body coil and whole mode gradient. Note that the readout bandwidth was increased to minimize the effect of B_0 inhomogeneity (Table 1). For each case, both non-iterative (Eq. 13) and iterative (Eq. 12) NUFFT-based reconstructions were performed. Iterative NUFFT-based reconstruction was performed via CG iteration, initialized with an all-zero image, and executed for 5 iterations.

Standard GNL-correction via image-domain interpolation was also performed as a reference. All reconstructed images were sinc interpolated (to 1024×1024 points) for display.

To compare the performance of the standard and proposed GNL-correction strategies, a series of GNL-corrections of the HR insert plane (axial) of the ACR phantom placed at different off-isocenter positions was also performed. For all 13 cases, standard GNL-correction via image-domain interpolation and the proposed non-iterative NUFFT-based correction reconstruction (Eq. 13) were performed with zoom gradient mode. Again, all reconstructed images were sinc interpolated (4× magnification) for display. Some commercial scanners also have the option of sinc interpolating (by zero-padding the *k*-space data) uncorrected images prior to GNL-correction, a process similar to the oversampled FFT component of our non-iterative NUFFT-based correction reconstruction. To investigate the effect of this action, uncorrected images were 4× sinc interpolated prior to standard GNL-correction. For consistency, *k*-space data was also 4× zero-padded prior to NUFFT-based correction reconstruction. We highlight that the notion of zero-padding *k*-space prior to NUFFT-based reconstruction is generally only relevant for fully-sampled acquisitions, so this step will not be applied to later iterative reconstructions of undersampled data.

The images of the ACR phantom were assessed by five independent observers to determine whether a significant difference between the resolution performance of the standard and proposed GNL-correction methods can be detected. The HR insert of the ACR phantom contains three groups of resolution inserts (dots) corresponding to nominal resolution values of 0.9, 1.0 and, 1.1 mm. The total number of resolution dots is 93, with 31 dots in each group. For each group, the numbers of dots that were distinguishable in images before and after correction were recorded by each observer. A dot was regarded as distinguishable if it could be visually distinguished from surrounding dots in all four directions (up/down/right/left). This criterion is somewhat more strict than the standard ACR QA resolution criteria, which states that the resolution of a certain group is reached provided all 4 dots in at least one row are recognizable as points of greater signal intensity than the spaces between them (30). Statistical significance between assessor values of the different correction results was determined via one-sided Wilcoxon signed-rank tests in both directions.

In addition to the manual evaluation process described above, resolution insert contrast was automatically measured from line profiles over four resolution dots in the 1.0 mm group to provide a separate, objective measure of correction performance. Within each line profile, the four peaks corresponding to the four resolution dots were automatically identified, along with the minimum valley point between each (three total). Insert contrast was measured as the smaller intensity difference between a peak and its adjacent valley points. In some cases, blurring causes peaks to merge such that all four are not distinguishable – for such cases, insert contrast was set to zero.

For the ACR phantom data acquired at -47 mm, each repetition was reconstructed without GNLC, or via either the standard or proposed NUFFT-based correction strategy. The two images were then subtracted to remove image content, and the 2D power spectrum of the residual noise was calculated by discrete Fourier transformation (DFT) of the 2D autocorrelation function of a 100×100 points kernel located at the center of the difference

image. This 2D spectrum was then averaged along one dimension to yield a 1D profile for visualization.

A single 2D axial slice of the fully-sampled T_2-weighted data set located at +39 mm superior of gradient isocenter was also reconstructed using both the standard GNL-correction method and the proposed non-iterative NUFFT-based strategy to investigate the relative performance of these methods *in vivo* under standard imaging conditions. All GNL-corrections were performed coil-by-coil for this multi-channel data set, and subsequently 2× sinc interpolated and root-sum-of-squares combined for display.

To investigate the utility of our proposed framework for accelerated imaging applications, a single slice from the MP-RAGE data set located at +59 mm superior of gradient isocenter (within standard clinical coverage) was uniformly undersampled (3×) in the in-plane phase encoding direction to simulate a 2D SENSE-type reconstruction (23). Coil sensitivity profiles were estimated from separate calibration scan data via ESPIRiT (31). Two separate reconstruction experiments were performed using SENSE signal model with Tikhonov regularization (Tikhonov-SENSE), as described in Eq. 15. In both cases, CG iteration was used to solve the optimization problem, and executed for 20 iterations with $\lambda = 0.01$ (manually selected). In the first reconstruction experiment, the forward operator, **A**, was defined as a standard DFT, and standard GNL-correction was performed on the reconstructed image. In the second experiment, **A** was defined as the NUFFT (as in Eq. 9) such that GNL was accounted for during image reconstruction. *In vivo* images were 2× sinc interpolated for display.

Similar to the previous *in vivo* example, the T_2-weighted image data set located at +35 mm superior of gradient isocenter was also retrospectively undersampled in the phase-encoded dimension albeit according to a variable-density random distribution (2×). Two separate reconstruction experiments were performed using CLEAR signal model with LLR regularization (22), as described in Eq. 16. In both cases, image blocks of width 8 and $\lambda = 0.002$ (manually selected) were used, and the nonlinear optimization problem was solved via 100 iterations of Nesterov's optimal gradient method (32, 33). As in the above SENSE example, one experiment was performed with **A** defined as a standard DFT, with subsequent coil-by-coil standard GNL-correction, and the second was performed with **A** defined as the distortion field-based NUFFT. All multi-channel data sets were individually 2× sinc interpolated and then root-sum-of-squares combined for display.

Results

Iterative Reconstruction vs. Non-iterative Approximation

Fig. 1 shows images derived from fully-sampled ACR phantom data. Each row corresponds to the HR insert plane of the phantom located at two axial positions (a-d: -82 mm, e-h: -122 mm) with zoom gradient mode. Listed from left to right in each row are: uncorrected (a, e); standard GNL-correction via image-domain interpolation (b, f); NUFFT-based non-iterative GNL-correction (c, g); and NUFFT-based iterative GNL-correction (d, h). An enlargement of the HR insert area of each image is shown below its corresponding full-scale image. Comparing Fig. 1(a) and 1(e) highlights the varying effect of GNL as a function of imaging

plane distance from magnet isocenter. Fig. 2 shows an example of large distortion using whole body mode gradient, with the same layout as that of Fig. 1. The imaging plane was located at -235 mm in S/I direction, near the edge of whole body gradient mode FOV. In both Figs. 1 and 2, no substantial visual difference between the non-iterative and iterative NUFFT-based corrections was observed, suggesting that the non-iterative approximation is an efficient alternative to solving the complete inverse problem for fully-sampled Cartesian MRI. Additionally, in all scenarios the NUFFT-based corrections exhibited less spatial blurring and distortion than the standard GNL-correction results.

GNL-Correction Performance vs. Distance From Magnet Isocenter

Fig. 3 shows enlargements of the ACR phantom HR inserts from the results of standard and proposed NUFFT-based GNL-corrections, with the purpose of demonstrating how correction performance degrades as a function of distance from magnet isocenter. Noting the results shown in Figs. 1 and 2, only the non-iterative NUFFT-based correction results are included. The physical scanning locations (relative to isocenter along the S/I direction) of the HR insert slices are indicated by the "distance" axis. Only images acquired beyond 77 mm from isocenter are shown since resolution dot resolvability was not substantially degraded at closer scan locations. Images in the first two rows were first GNL-corrected and then sinc interpolated for display. As discussed in the previous section, images in the third and fourth rows were either sinc interpolated (for the standard approach) or zero-padded in *k*-space (for the proposed approach) prior to GNL-correction. In all cases, both the standard and proposed GNL-correction methods exhibit progressively degraded resolution as the imaging plane is offset farther from magnet isocenter. This is illustrated by the gradually-increased blurring of resolution dots in each row of Fig. 3. However, in both scenarios (sinc interpolated before or after GNL-correction), the resolution degradation of the proposed approach is reduced compared to that of the standard image-domain interpolation strategy. The discrepancy exists even when sinc interpolation is performed prior to GNL-correction, which highlights the importance of deapodization operations inherent to the NUFFT.

Fig. 4(a) shows the average resolution scores (indicated by the number of resolution dots in HR inserts that are distinguishable) of the five human observers for the HR inserts in Fig. 3 versus imaging plane locations for each GNL-correction method. Error bars are also included to show the standard deviations in the observer scores. The scores of two standard GNL-correction groups drop substantially faster than the two NUFFT-based correction groups, especially for distances above 100 mm. Sinc interpolation before GNL-correction does offset some improvements in performance over the base case; however, it is still less effective than the two NUFFT based methods especially when GNL is strong (after 100 mm). The scores of the two NUFFT-based correction groups were found to be significantly higher (one-sided Wilcoxon signed-rank tests; $P < 0.05$) than their standard counterparts beyond a certain distance from isocenter ($d > 82$ mm for the regular cases, and $d > 102$ mm for the cases when sinc interpolation was performed prior to correction). At all distances, reversed one-sided tests failed to show that the standard corrections had higher scores than the NUFFT-based corrections.

Fig. 4(b) shows line profiles across resolution dots in the 1.0 mm resolution insert group that were automatically analyzed as a separate, objective measure of performance. Due to the blurring effect of interpolation, insert prominence is decreased in the two standard GNL-correction groups, reflecting a decrease in insert contrast. Fig. 4(c) shows the results of automated insert contrast analysis for these line profiles for images acquired at various distances from isocenter. Note that insert contrast for the two standard GNL-correction groups drop substantially faster than for the two NUFFT-based groups, and in a manner consistent with the manual scoring results in Fig. 4(a).

Fig. 5 displays the noise power spectra calculated from subtracted images of the standard GNL-correction, non-iterative NUFFT, and the image without GNL-correction. As expected, the power spectrum of the uncorrected image appears like white noise, mostly uniform except for some low frequency content that can be attributed to phase changes from field drift between scans. Compared to this, the spectrum of standard GNL-correction image exhibits degradation in its high frequency components – like it has been low-pass filtered – and highlights the smoothing effects of interpolation-based GNL correction. This corroborates the image resolution loss observed in our phantom results. Note that the spectrum of the proposed NUFFT-based correction image does not exhibit this same loss, since the NUFFT implicitly counters (via deconvolution) any blurring introduced by interpolation (Eq. 9).

In Vivo Reconstruction Results

Fig. 6 shows reconstructed images for the fully-sampled, multi-channel T_2-weighted image data before and after both standard and the proposed non-iterative NUFFT-based GNL-correction. Even relatively close to isocenter (+39 mm S/I) there still is noticeable geometric distortion in the uncorrected image (see arrows). A visual comparison between Fig. 6(b) and (c) reveals that while both approaches provide the same coarse-scale geometric correction, the proposed NUFFT-based approach better preserves the subtle texture of the cerrebellar gyri as well as the morphology of vascular structures. As highlighted by the arrows in the images, the interpolation operations underlying standard GNL-correction undesirably smooth out some of these anatomical details. The standard GNL-correction results in loss of vessel wall clarity (arrow b) compared with reconstruction before correction (arrow a) and NUFFT-based approach (arrow c). Fig. 7 shows the subtracted difference between Figs. 6(b) and 6(c). The difference image is multiplied by 10, and displayed in the same window/level. Fig. 7 highlights that the differences between the images corrected by standard GNL-correction and the proposed NUFFT-based correction are mainly high spatial frequency components including the boundaries and small structures, which is consistent with our previous phantom results and power spectra analysis in Fig. 5.

Fig. 8 shows Tikhonov-SENSE-type reconstructions of the (retrospectively) 3× uniformly undersampled reconstruction of the MP-RAGE data set. Fig. 8(a) shows a standard SENSE reconstruction without GNL-correction. Fig. 8(b) shows the the result of performing standard image-domain GNL-correction on the result from Fig. 8(a). Fig. 8(c) shows the result of an NUFFT-based SENSE reconstruction with integrated GNL-correction. Although geometric distortion at this position (+59 mm S/I) is subtle, the standard GNL-correction

degrades the spatial resolution of the uncorrected image. Conversely, the correction generated using our proposed strategy does not exhibit this blurring. These differences are especially apparent at the gray matter/white matter boundaries, as indicated by the arrows in Fig. 8. The cortical white matter junction is better depicted before GNL-correction (arrow a) and with integrated NUFFT (arrow c) than with standard GNL-correction (arrow b). Also note that the proposed correction strategy (Fig. 8(c)) preserves the noise level and texture of the uncorrected image, whereas the interpolation operations inherent to the standard GNL-correction alter this as well as compromise morphology. Since both noise and image details are subtle structures, we believe it is better to retain all information available and let the user separately "denoise" the result if they desire to do so.

Fig. 9 shows CLEAR reconstructions of the (retrospectively) 2× variable density random undersampled reconstruction of a different slice of the T_2-weighted image data. Fig. 9(a) shows a standard CLEAR reconstruction without GNL-correction and Fig. 9(b) shows the result of applying standard GNL-correction to Fig. 9(a). Fig. 9(c) shows the result of an NUFFT-based CLEAR reconstruction with integrated GNL-correction. Similar to fully-sampled and SENSE-type undersampled reconstructions in Figs. 6 and 8, the NUFFT-based result in Fig. 9(c) provides comparable coarse-scale geometric correction to the standard approach in Fig. 9(b) but better preserves the subtle structures in the cerebellar region and sharpness of small vessels. Note that blurring of the cerebellar folia occurs with standard GNL-correction (arrow b) compared with the result before GNL-correction (arrow a) and utilizing integrated NUFFT (arrow c).

Discussion

In this study, we propose a new GNL-correction strategy for conventional MR imaging that accounts for the effects of GNL during – rather than after – reconstruction to the image domain. Standard GNL-correction, which is based on strict image-domain interpolation, can effectively correct geometric distortion but at the expense of reduced spatial resolution from the (unaccounted for) smoothing effects of interpolation. Additionally, since those methods are derived under continuous image assumptions, operating on discretized images can also introduce localized distortion in extreme GNL cases. As demonstrated in Fig. 3, performing sinc interpolation before standard GNL-correction partially compensates for these issues, but does not entirely overcome them, especially where stronger distortion is present. Our proposed NUFFT-based GNL-correction and image reconstruction framework prospectively accounts for both image discretization and interpolation-based spatial blurring (via deapodization), and is correspondingly able to better alleviate resolution loss and local distortion while still correcting coarse-scale geometric distortion. The resolution-preserving capability of our approach is visually apparent in the phantom results shown in Figs. 1 to 4, especially when the imaging plane is located farther away from isocenter where stronger GNL presents. As demonstrated in Figs. 6 to 9, for *in vivo* exams our proposed GNL-correction strategy similarly better preserves fine anatomical details such as small vessel morphology and sharp tissue boundaries.

The improved capability offered by the proposed NUFFT-based method can potentially benefit any MRI application where GNL-correction is routinely performed. However, we

believe these subtle but concrete benefits will be particularly important in applications that require precise morphological or volumetric measurements, such as Alzheimer's disease characterization (5) and treatment planning (6, 7), or where the region of interest extends across a large FOV (4). Another potential application of the proposed methodology is moving table whole-body imaging, where GNL-correction is especially challenging since each *k*-space measurement is made at a slightly different displacement between the moving object and the gradient field (34). Although the proposed method was tested within a ±120 mm FOV, the maximum FOV of the zoom gradient is ±175 mm, so the gradient distortion was not maximized. The resolution preserving effect of the proposed method is expected to be more significant in this extended region, as suggested by the large distortion example acquired at the edge of FOV with the whole body mode gradient in Fig. 2. The proposed NUFFT-based GNL-correction strategy may also be very beneficial for emerging MRI scanner architectures, such as high-performance head-only systems (35) where GNL could be more pronounced.

As demonstrated in this work, the proposed GNL-correction strategy can be applied to both routine imaging protocols with fully sampled *k*-space data and accelerated acquisitions. When it is applied to fully sampled data, one can either compute the full iterative solution of Eq. 12 or employ the non-iterative NUFFT-based approximation in Eq. 13 as a minimal computational load alternative. As shown, the latter approach is of similar computational cost to standard GNL-correction but offers superior performance. For accelerated imaging scenarios, our proposed strategy can be readily integrated into advanced reconstruction models like Tikhonov-SENSE (Eq. 15) and CLEAR (Eq. 16) by replacing their standard forward and adjoint FFT with NUFFT operators. Although the NUFFT and standard FFT have the same computational complexity order (19), NUFFTs are more expensive to compute due to their internal interpolation operations. While not a substantial concern for non-iterative methods, the additional computational cost of performing NUFFTs does increase the total execution times for iterative reconstruction methods. In this study, we observed that employing NUFFTs with small oversampling factors (1.25×) and kernel sizes (5 points) gave robust performance while minimizing the added computation load. For example, generating the 256×256 Tikhonov-SENSE results in Fig. 8 via 20 CG iterations on the computing system described in Methods with the standard FFT and NUFFT setups required only 0.65 sec and 2.00 sec, respectively. Thus, the added expense is non-trivial but the approach remains practical.

Beyond application to different MRI areas and within alternative reconstruction models (e.g., sparsity-based), several extensions of the proposed framework will be examined in the future. Although all examples in this work demonstrate 2D in-plane GNL-correction for Cartesian imaging, the proposed framework readily applies for oblique scan and full 3D volume GNL-correction. The proposed GNL-correction framework can also be extended for (both 2D and 3D) non-Cartesian acquisitions by migrating from type I to type III NUFFT's (36), similar to the pathway taken by Knoll et al. (21) for radial PATLOC acquisitions. Spatial smoothing penalties like total variation can be used within Eq. 11 to prospectively combat noise during GNL-corrected reconstruction while offering a degree of image structure preservation. Finally, for all iterative reconstruction results presented in this work,

the regularization parameter, λ, was selected manually following visual assessment of image results. In future studies, we hope to automate and optimize this selection process based on concrete image quality metrics like low contrast object detectability (37) or mean-square error (38) to eliminate the potential for subjectivity and ensure maximally fair comparisons.

Conclusion

In this work, a new GNL-correction framework for conventional MR imaging is proposed and demonstrated to better preserve spatial resolution than the conventional image-domain interpolation strategy. The proposed framework is general and can be applied for both non-accelerated and accelerated acquisitions.

Acknowledgments

The authors would like to thank Paul Weavers for reviewing the ACR phantom data.

Funding Support: NIH R01EB010065, NIH R21EB017840

*Bibliography

1. Harvey PR, Katznelson E. Modular gradient coil: a new concept in high-performance whole-body gradient coil design. Magn Reson Med. 1999; 42:561–570. [PubMed: 10467301]
2. O'Donnell M, Edelstein WA. NMR imaging in the presence of magnetic field inhomogeneities and gradient field nonlinearities. Med Phys. 1985; 12:20–26. [PubMed: 3974521]
3. Baldwin LN, Wachowicz K, Thomas SD, Rivest R, Fallone BG. Characterization, prediction, and correction of geometric distortion in 3T MR images. Med Phys. 2007; 34:388–399. [PubMed: 17388155]
4. Doran SJ, Charles-Edwards L, Reinsberg SA, Leach MO. A complete distortion correction for MR images: I. Gradient warp correction. Phys Med Biol. 2005; 50:1343–1361. [PubMed: 15798328]
5. Gunter JL, Bernstein MA, Borowski BJ, Ward CP, Britson PJ, Felmlee JP, Schuff N, Weiner M, Jack CR. Measurement of MRI scanner performance with the ADNI phantom. Med Phys. 2009; 36:2193–2205. [PubMed: 19610308]
6. Schad LR, Ehricke HH, Wowra B, Layer G, Engenhart R, Kauczor HU, Zabel HJ, Brix G, Lorenz WJ. Correction of spatial distortion in magnetic resonance angiography for radiosurgical treatment planning of cerebral arteriovenous malformations. Magn Reson Imaging. 1992; 10:609–621. [PubMed: 1501531]
7. Chen Z, Ma CM, Paskalev K, Li J, Yang J, Richardson T, Palacio L, Xu X, Chen L. Investigation of MR image distortion for radiotherapy treatment planning of prostate cancer. Phys Med Biol. 2006; 51:1393–1403. [PubMed: 16510951]
8. Glover GH, Pelc NJ. General Electric Company. Method for correcting image distortion due to gradient nonuniformity. US Patent 4,591,789. May 27.1986
9. Bernstein, MA.; King, KF.; Zhou, XJ. Handbook of MRI pulse sequences. Burlington (MA): Elsevier Academic Press; 2004.
10. Thévenaz P, Blu T, Unser M. Interpolation revisited. IEEE Trans Med Imaging. 2000; 19:739–758. [PubMed: 11055789]
11. Slavens, ZW.; Hinks, RS.; Polzin, JA.; Johnson, MT. Improved MR image magnification by generalized interpolation of complex data. Proceedings of the 15th Annual Meeting of the ISMRM; Berlin, Germany. 2007; p. 1887
12. Fessler JA, Lee S, Olafsson VT, Shi HR, Noll DC. Toeplitz-based iterative image reconstruction for MRI with correction for magnetic field inhomogeneity. IEEE Trans on Signal Proc. 2005; 53:3393–3402.

13. Reeder SB, Pineda AR, Wen Z, Shimakawa A, Yu H, Brittain JH, Gold GE, Beaulieu CH, Pelc NJ. Iterative decomposition of water and fat with echo asymmetry and least-squares estimation (IDEAL): application with fast spin-echo imaging. Magn Reson Med. 2005; 54:636–644. [PubMed: 16092103]
14. Hennig J, Welz AM, Schultz G, Korvink J, Liu Z, Speck O, Zaitsev M. Parallel imaging in non-bijective, curvilinear magnetic field gradients: a concept study. Magn Reson Mater Phy. 2008; 21:5–14.
15. Stockmann JP, Ciris PA, Galiana G, Tam L, Constable RT. O-space imaging: highly efficient parallel imaging using second-order nonlinear fields as encoding gradients with no phase encoding. Magn Reson Med. 2010; 64:447–456. [PubMed: 20665789]
16. Trzasko, JD.; Tao, S.; Shu, Y.; Manduca, A.; Bernstein, MA. Integrated image reconstruction and gradient nonlinearity correction. Proceedings of the 22th Annual Meeting of the ISMRM; Milan, Italy. 2014; p. 4847
17. Fessler JA. Model-based image reconstruction for MRI. IEEE Signal Process Mag. 2010; 27:81–89. [PubMed: 21135916]
18. Greengard L, Lee JY, Inati S. The fast sinc transform and image reconstruction from nonuniform samples in *k*-space. Comm App Math Comp Sci. 2006; 1:121–131.
19. Fessler JA, Sutton BP. Nonuniform fast Fourier transforms using min-max interpolation. IEEE Trans Signal Proc. 2003; 51:560–574.
20. Beatty PJ, Nishimura DG, Pauly JM. Rapid gridding reconstruction with a minimal oversampling ratio. IEEE Trans Med Imaging. 2005; 24:799–808. [PubMed: 15959939]
21. Knoll F, Schultz G, Bredies K, Gallichan D, Zaitsev M, Hennig J, Stollberger R. Reconstruction of undersampled radial PatLoc imaging using total generalized variation. Magn Reson Med. 2013; 70:40–52. [PubMed: 22847824]
22. Trzasko, JD.; Manduca, A. Local versus global low-rank promotion in dynamic MRI series reconstruction. Proceedings of the 19th Annual Meeting of the ISMRM; Montreal, Canada. 2011; p. 4371
23. Pruessmann KP, Weiger M, Scheidegger MB, Boesiger P. SENSE: sensitivity encoding for fast MRI. Magn Reson Med. 1999; 42:952–962. [PubMed: 10542355]
24. Trzasko, JD.; Manduca, A. CLEAR: calibration-free parallel imaging using locally low-rank encouraging reconstruction. Proceedings of the 20th Annual Meeting of the ISMRM; Melbourne, Australia. 2012; p. 517
25. Wilm BJ, Barmet C, Pavan M, Pruessmann KP. Higher order reconstruction for MRI in the presence of spatiotemporal field perturbations. Magn Reson Med. 2011; 65:1690–1701. [PubMed: 21520269]
26. Janke A, Zhao H, Cowin GJ, Galloway GJ, Doddrell DM. Use of spherical harmonic deconvolution methods to compensate for nonlinear gradient effects on MRI images. Magn Reson Med. 2004; 52:115–122. [PubMed: 15236374]
27. Tao, S.; Trzasko, JD.; Gunter, JL.; Lee, SK.; Tan, ET.; Shu, Y.; Thostenson, KB.; Bernstein, MA. Measurement and correction of gradient nonlinearity by spherical harmonic fitting using the ADNI phantom. Proceedings of the 22th Annual Meeting of the ISMRM; Milan, Italy. 2014; p. 4863
28. Wang D, Doddrell DM, Cowin G. A novel phantom and method for comprehensive 3-dimensional measurement and correction of geometric distortion in magnetic resonance imaging. Magn Reson Imaging. 2004; 22:529–542. [PubMed: 15120173]
29. Baldwin LN, Wachowicz K, Fallone BG. A two-step scheme for distortion rectification of magnetic resonance images. Med Phys. 2009; 36:3917–3926. [PubMed: 19810464]
30. Phantom test guidance for the ACR MRI accreditation program. Reston: The American College of Radiology; Reston, Virginia: 2005.
31. Uecker M, Lai P, Murphy MJ, Virtue P, Elad M, Pauly JM, Vasanawala SS, Lustig M. ESPIRiT–an eigenvalue approach to autocalibrating parallel MRI: where SENSE meets GRAPPA. Magn Reson Med. 2014; 71:990–1001. [PubMed: 23649942]
32. Nesterov Y. A method of solving a convex programming problem with convergence rate O (1/k2). Sov Math Dokl. 1983; 27:372–376.

33. O'Donoghue B, Candes E. Adaptive restart for accelerated gradient schemes. Found Comput Math. 201310.1007/s10208-013-9150-3

34. Polzin JA, Kruger DG, Gurr DH, Brittain JH, Riederer SJ. Correction for gradient nonlinearity in continuously moving table MR imaging. Magn Reson Med. 2004; 52:181–187. [PubMed: 15236384]

35. Mathieu, JB.; Lee, SK.; Budesheim, EG.; Hua, Y.; Lin, J.; Immer, C.; Lechner-Greite, SM.; Piel, J.; Schenck, JF.; Bernstein, MA.; Huston, J.; Foo, TK. Preliminary evaluation of a high performance gradient coil for 3T head specialty scanner. Proceedings of the 21th Annual Meeting of the ISMRM; Salt Lake City, USA. 2013; p. 2708

36. Lee JY, Greengard L. The type 3 nonuniform FFT and its applications. J Comput Phys. 2005; 206:1–5.

37. Trzasko JD, Bao Z, Manduca A, McGee KP, Bernstein MA. Sparsity and low-contrast object detectability. Magn Reson Med. 2012; 67:1022–1032. [PubMed: 22105698]

38. Stein CM. Estimation of the mean of a multivariate normal distribution. Ann Stat. 1981; 9:1135–1151.

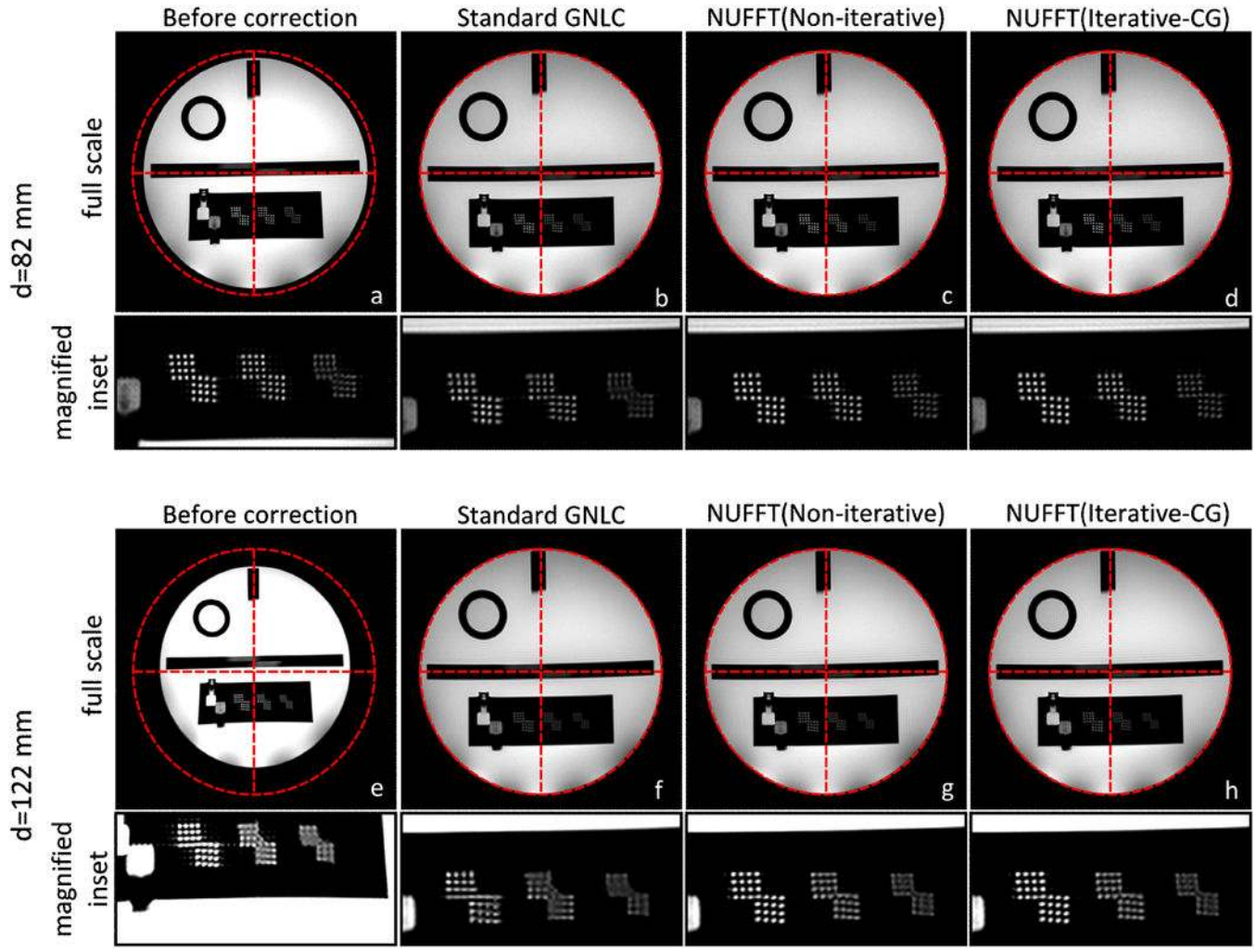

Figure 1.

ACR phantom images acquired with zoom gradient mode (full scale and enlarged resolution inserts) before and after GNL-correction. (a) and (e): images acquired at -82 and -122 mm in the S/I direction, respectively; (b) to (d) and (f) to (h): images corrected with Standard GNL-correction (Standard GNLC), non-iterative NUFFT operator (NUFFT Non-iterative), and iterative reconstruction with incorporated NUFFT solved by CG (NUFFT iterative-CG).

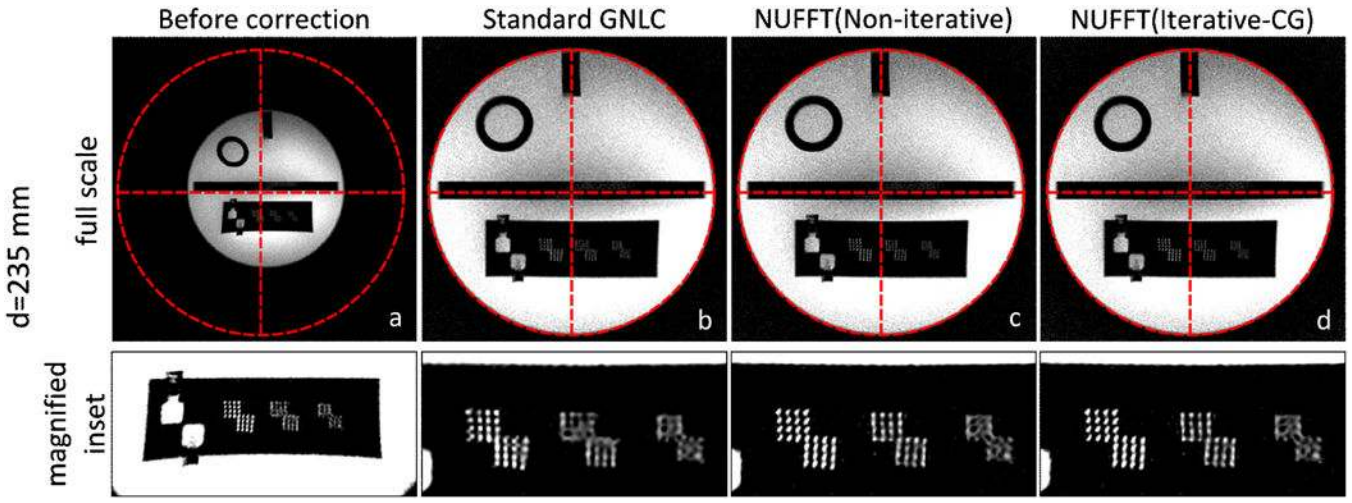

Figure 2.

ACR phantom images acquired with whole body gradient mode (full scale and enlarged resolution inserts) before and after GNL-correction. (a): image acquired at -235 mm in the S/I direction; (b) to (d): images corrected with Standard GNL-correction (Standard GNLC), non-iterative NUFFT operator (NUFFT Non-iterative), and iterative reconstruction with incorporated NUFFT solved by CG (NUFFT iterative-CG). Note that the whole body coil was used instead of the head coil in Fig. 1 since the slice location was far out of the coverage of the head coil.

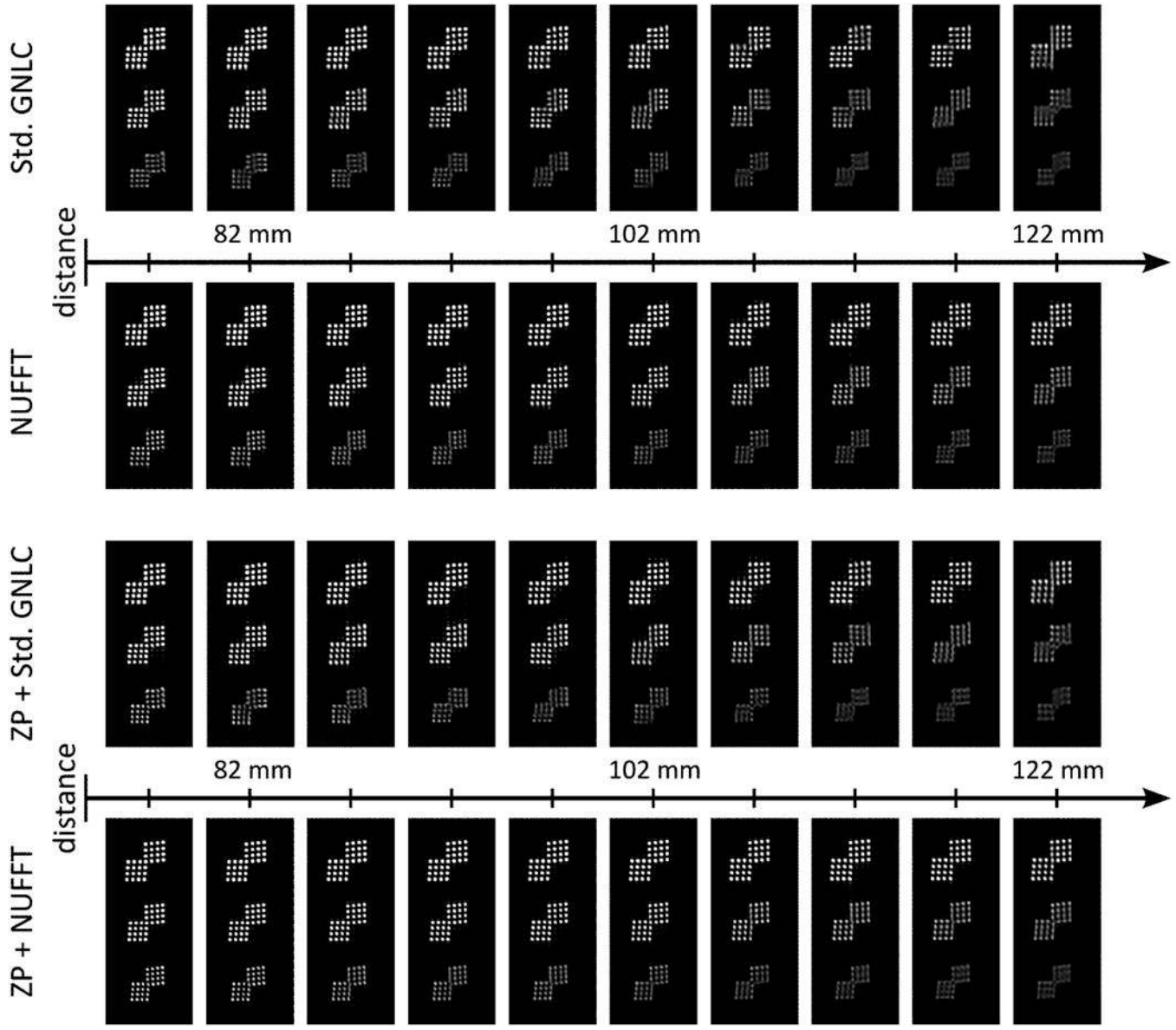

Figure 3.

Effects of resolution degradation versus distance from magnet isocenter. The “distance” axis indicates the locations in S/I direction where the corresponding images were acquired. The first and second rows shows the resolution inserts regions of the images corrected with Standard GNL-correction (Std. GNLC) and non-iterative NUFFT (NUFFT). The images were then sinc interpolated (4×) to show details. In the third and fourth rows, images were first sinc interpolated (zero padded in *k* space) by a factor of 4 and then corrected with Std. GNLC and NUFFT, respectively.

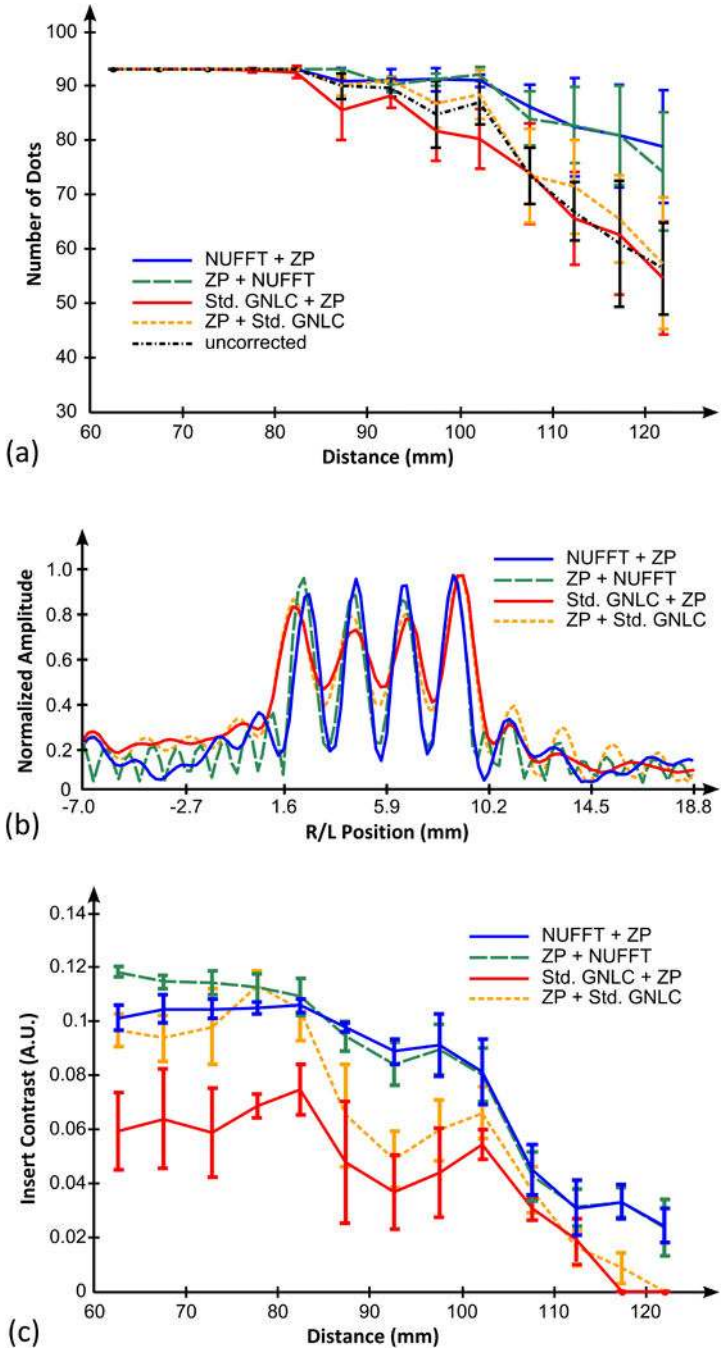

Figure 4.

(a) Imaging plane location versus resolution scores of each correction method in Fig. 3. The resolution scores are defined as the total number of resolution dots that are distinguishable in all the four directions (up/down/right/left). For NUFFT+ZP and Std. GNLC+ZP group, the images being scored are first corrected with the corresponding methods and then sinc interpolated (zero padded in *k* space) to compare image detail. For ZP+NUFFT and ZP+Std. GNLC group, the order of zero padding and GNL-correction is reversed; (b) Representative examples of the line profiles across four resolution dots (in the 1.0 mm resolution inserts

group) in images corrected with each GNL-correction method; (c) insert contrast measured from line profiles in images acquired at various distances from isocenter. Insert contrast is here defined as the distance between each of the four peaks (corresponding to four resolution dots) and the highest valley point next to it.

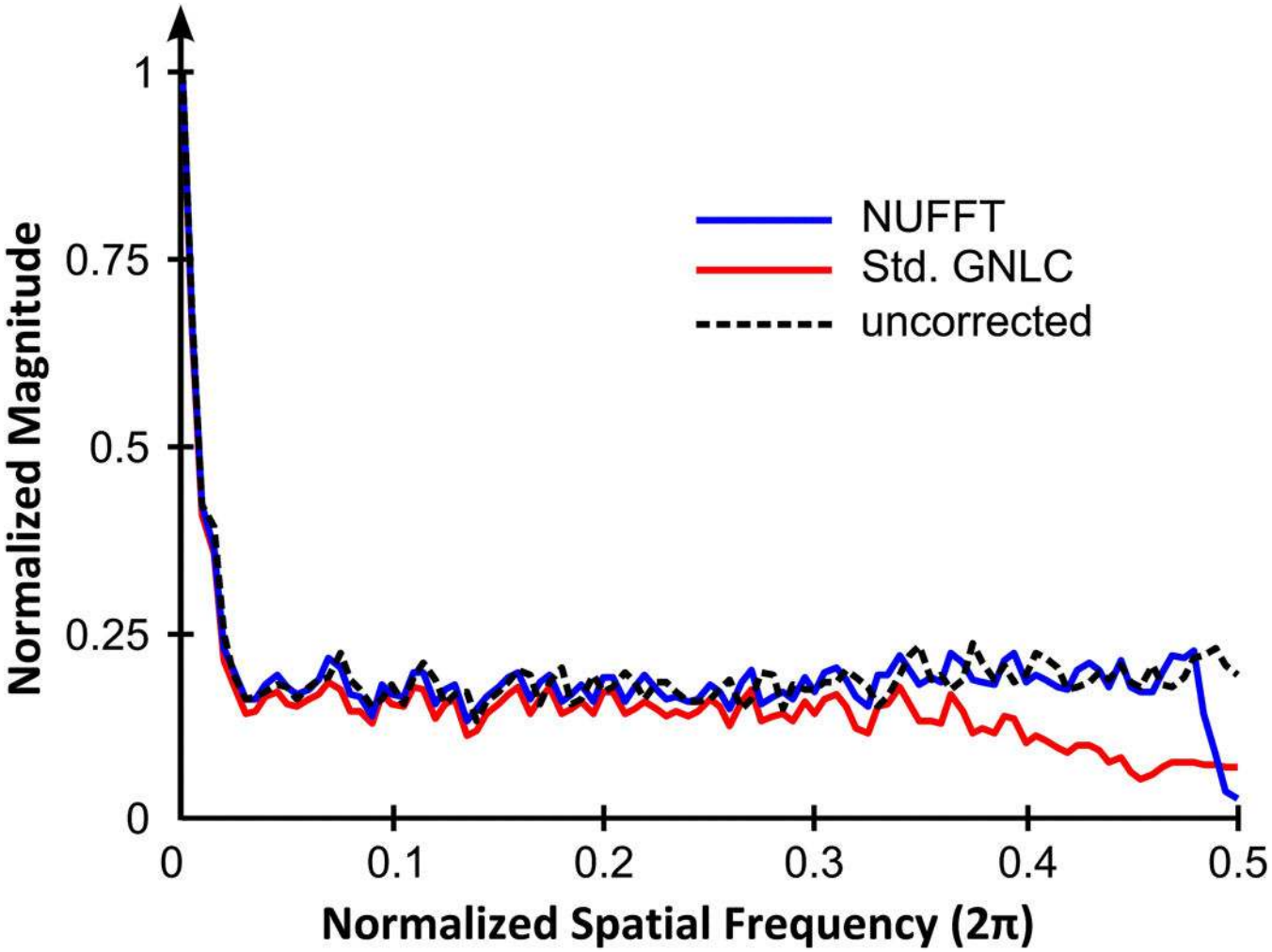

Figure 5.
Noise power spectra calculated from the subtractions of two separate images (ACR phantom) acquired at the same slice location, obtained without GNL correction, with standard GNL-correction (Std. GNLC), or with non-iterative NUFFT-based GNL-correction (NUFFT).

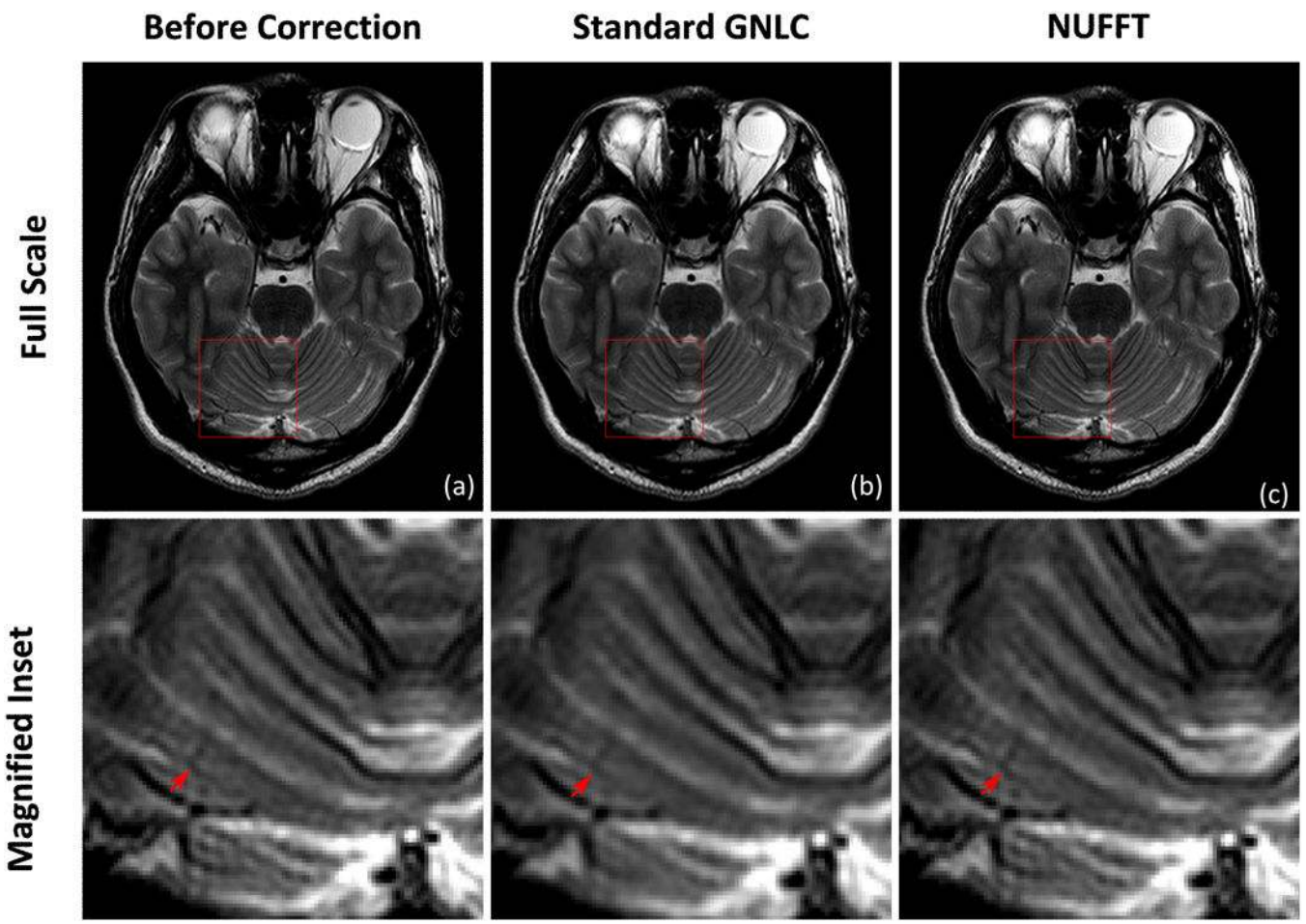

Figure 6.

Example of T_2-weighted SE images (volunteer 1) reconstructed with fully sampled *k*-space data. (a) image before GNL-correction; (b) image corrected by Standard GNL-correction, and (c) image corrected by the proposed non-iterative NUFFT approach. Note that small vessel wall features (arrow) apparent in the uncorrected image (a) are preserved by the proposed GNL-correction strategy (c) but distorted during standard correction.

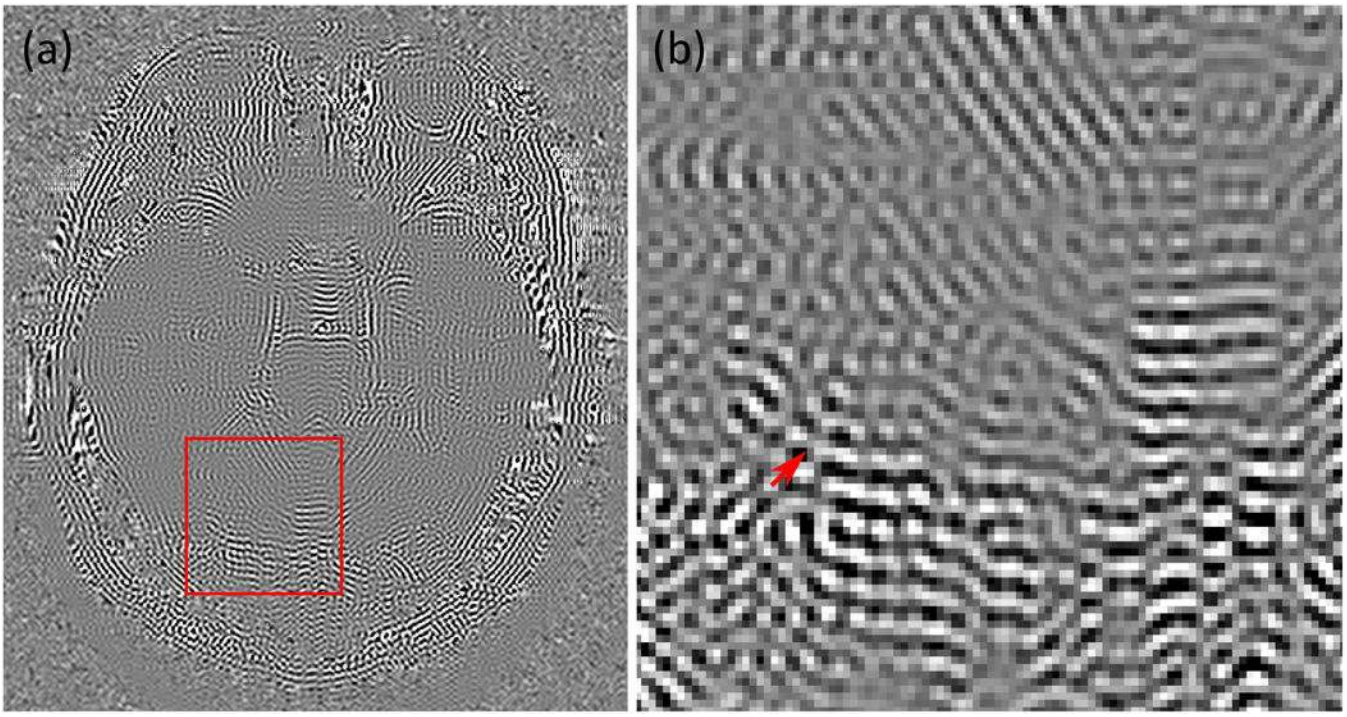

Figure 7.

Difference (10× magnitude amplification) between Fig. 6(b) and 6(c) in full scale (a) and magnified inset (b). The arrow points to the same location as those in Fig. 6. Fig. 7 highlights that the differences between the images corrected by standard GNL-correction and the proposed NUFFT-based correction are mainly high spatial frequency components including the boundaries and small structures.

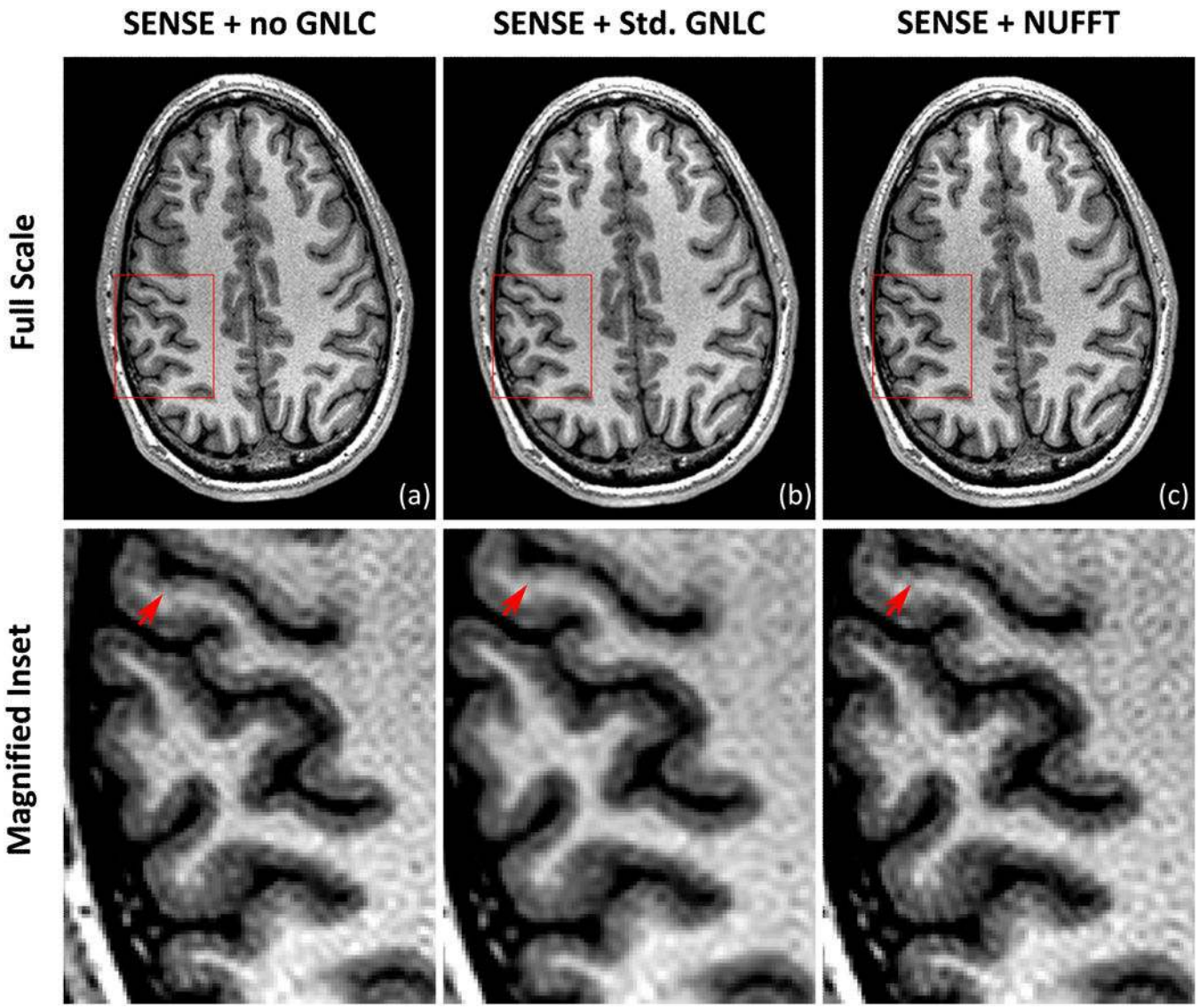

Figure 8.

Example of MP–RAGE images (volunteer 2) with SENSE-type reconstruction (3× uniformly subsampled in phase encoding direction). (a) image before GNL-correction; (b) image corrected by Standard GNL-correction, and (c) image corrected by iterative reconstruction with integrated NUFFT. Note that cortical white matter junctions (arrow) apparent in the uncorrected image are preserved by the proposed GNL-correction strategy (c) but distorted during standard correction.

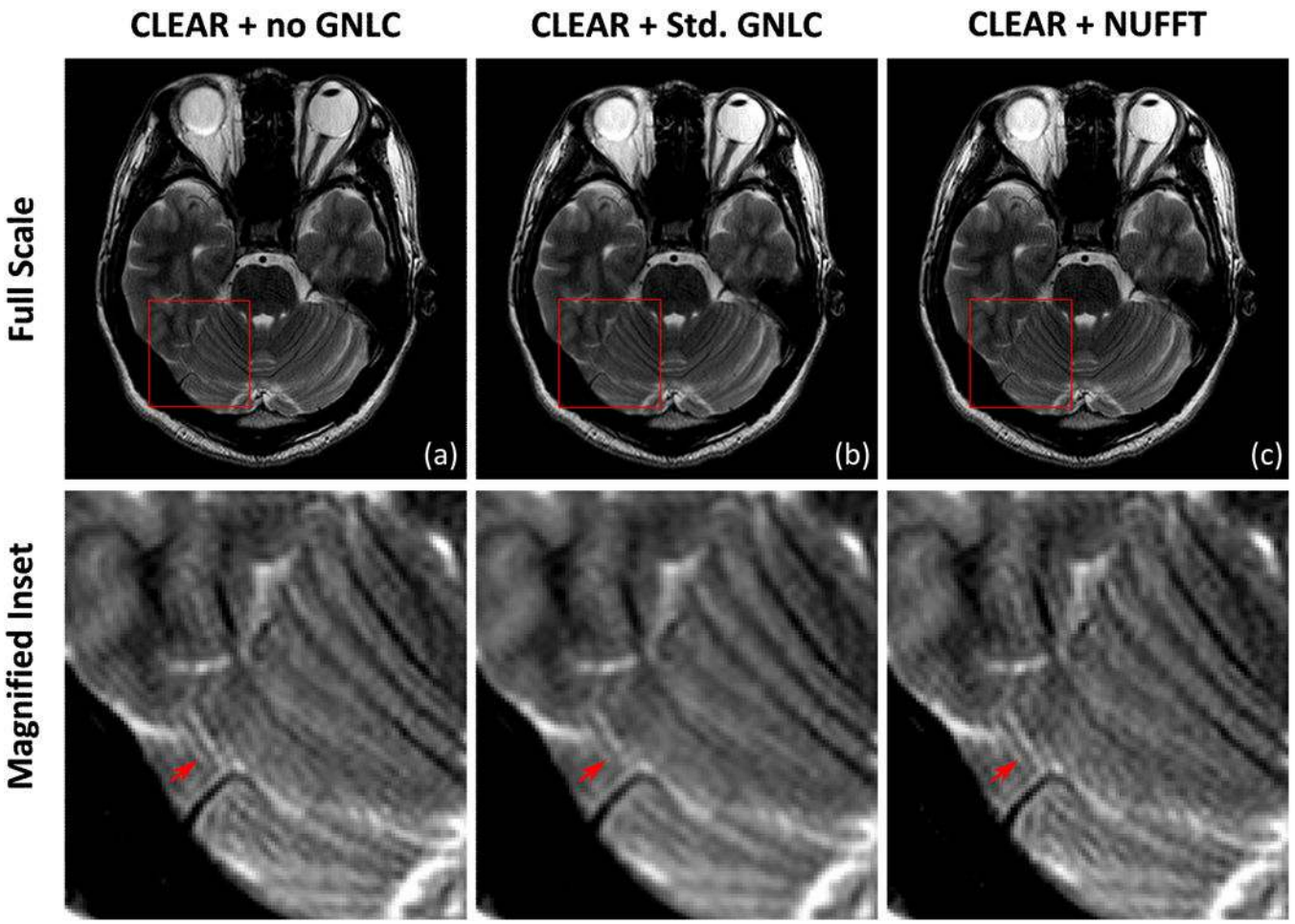

Figure 9.

Example of T_2-weighted SE images (volunteer 1) reconstructed with CLEAR (2× randomly subsampled in phase encoding direction). (a) image before GNL-correction; (b) image corrected by Standard GNL-correction, and (c) image corrected by iterative reconstruction with integrated NUFFT. Note that the cerebellar folia (arrow) apparent in the uncorrected image are preserved by the proposed GNL-correction strategy (c) but distorted during standard correction.

Table 1

Specifics of Protocols

Subject	ACR Phantom	ACR Phantom	*in vivo* Brain	*in vivo* Brain
Sequence	2D T_1 SE	2D T_1 SE	3D MP-RAGE	2D T_2 FSE
$FOV_x \times FOV_y (\times FOV_z)$	220×220 mm^2	210×210 mm^2	240×240(×240) mm^3	240×240 mm^2
$N_x \times N_y (\times N_z)$	256×256	384×384	256×256(×240)	256×256
TR/TE(/TI)	500/13 *msec*	500/10 *msec*	7/2.9(/900) *msec*	4800/105 *msec*
Flip Angle	90°	90°	8°	90°
Slice Thickness	3 mm	3 mm	1 mm	4 mm
Scan Plane	Axial	Axial	Axial	Axial
Bandwidth	±15.63 kHz	±83.33 kHz	±31.25 kHz	±25.00 kHz